Rev. Roum. Sci. Techn.– Électrotechn. et Énerg.
Vol. **63**, *1*, pp. 83–88, Bucarest, 2018

Dedicated to the memory of Academician Andrei Ţugulea

POLARIMETRIC RADAR IMAGE CLASSIFICATION USING DIRECTIONAL DIFFUSION AND DESCRIPTIVE STATISTICS

ROMULUS TEREBES[1], RAUL MALUTAN[1], MONICA BORDA[1], CHRISTIAN GERMAIN[2], LIONEL BOMBRUN[2], IOANA ILEA[1,2]

Key words: Radar, Polarimetry, Partial differential equations, Gray level co-occurrence matrix, Classification.

This paper proposes a novel denoising method for polarimetric synthetic aperture radar (PolSAR) image preprocessing tasks with integration and applications for texture-like land images classification tasks. The method is developed using the partial differential equations framework and employs a multi-polarimetric tensor to capture the geometry of fully polarimetric PolSAR data. The filtering intensity is modulated by the multiplicative gradient norm computed on the total scattered power. The method has good texture preservation properties and it is integrated on a PolSAR image classification chain providing good recognition accuracy rates. Visual results on real PolSAR data of maritime pine forests stands are also provided for showing its effectiveness.

1. INTRODUCTION

Airborne or spaceborne synthetic aperture radar (SAR) became nowadays one of the preferred tools for providing high resolution remote sensing images, being able to capture information irrespective of the weather conditions or of the day or night acquiring conditions. Operating in side-looking mode, such devices are able to capture the roughness of monitored terrains or oceans with spatial resolution ranging from centimeters to tenths of meters. SAR imaging devices can work and exploit multi-channel operation mode using techniques such as polarimetry and interferometry, or combinations of them, to provide rich and detailed information about the monitored area.

In this work we will refer only to polarimetric SAR (PolSAR) data obtained using horizontal and vertical polarized electromagnetic waves which are transmitted using active antennas placed on a moving platform. Reception antennas are used to record the polarimetric signature of the targets through the backscattered radiation, possibly repolarized. Such systems are capable of capturing texture-like, fine structure information, size and shape characterizing the targets within a resolution cell [1]. However, since the position of the scatterers within a cell varies, the received waves are coherent in frequency but not in phase, causing pixel-to-pixel variations in intensity, known as speckle. This type of noise has been shown to be multiplicative in nature and to have a negative impact on the accuracy of subsequent image segmentation or classification tasks [2].

A lot of methods for speckle reduction have been proposed recently in the literature. These methods are based on various mathematical formalisms ranging from adaptive weighting on oriented sliding windows [3, 4], region growing [5], non-local means and non-local neighborhoods [6–8], wavelet transforms [9], partial differential equations (PDE) [10–13]. Irrespective of the underlying mathematics, all these methods are conceived to eliminate speckle noise through local or non-local averaging operations, whilst preserving or even enhancing the high frequency important information such as edges and junctions.

Terrain classification is one of the main applications for PolSAR imaging allowing for subsequent analysis and interpretation steps for the rapidly accumulating data. For PolSAR data, most of these approaches are extended from the techniques developed for optical images and rely on descriptive statistics or on statistical models to capture textural and/or polarimetric information [14], without considering the data filtering step as a necessary prior for increased robustness.

The paper we are proposing extends the work in [12], giving full implementation details and studies its integration in a PolSAR image classification chain that exploits textural and polarimetric information for classifying filtered PolSAR data representing maritime pine tree forest stands of different ages.

The paper is organized as follows. In Section 2 we present our PDE-based filtering approach, its theoretical properties, numerical and implementation details. Section 3 introduces a classification framework for PolSAR images operating on the filtered data and using descriptive statistics extracted from a texture analysis step. Section 4 is dedicated to the experimental validation and present classification results on a real L band PolSAR image composed of maritime pine forest stands of different ages. The final section presents the conclusions of our work.

2. DIRECTIONAL DIFFUSION-BASED SPECKLE NOISE FILTERING

2.1. CONTINOUS MODEL

The PDE-based filtering approach that we are proposing operates on the polarimetric covariance matrix [3]. This matrix captures in each pixel the complex scattered amplitudes of the received PolSAR electromagnetic waves using horizontal (H) and vertical polarizations (V):

$$\boldsymbol{C}=\begin{bmatrix} |S_{HH}|^2 & \sqrt{2}S_{HH}S_{HV}^* & S_{HH}S_{VV}^* \\ \sqrt{2}S_{HV}S_{HH}^* & 2|S_{HV}|^2 & \sqrt{2}S_{HV}S_{VV}^* \\ S_{VV}S_{HH}^* & \sqrt{2}S_{VV}S_{HV}^* & |S_{VV}|^2 \end{bmatrix}. \quad (1)$$

[1] Technical University of Cluj-Napoca, 28 Memorandumului Street, Cluj-Napoca, Romania Email: Romulus.Terebes@com.utcluj.ro

[2] Université de Bordeaux, Laboratoire de l'Intégration du Matériau au Système, 351 Cours de la libération, 33405 Talence cedex, France

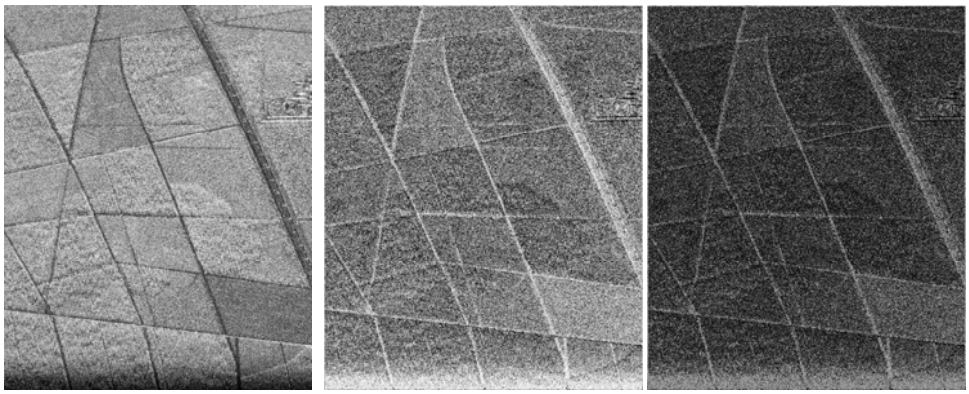

a) b) c)

Fig. 1 – Edge detectors on a real band L image (S_{HH} channel amplitude); a) original image (scaled down to 10 % of the initial size); b) Instantaneous coefficient of variation (ICOV); c) multiplicative gradient norm.

In (1) the first index denotes the received wave polarization state, the second index stands for the polarization of a transmitted wave and * indicates complex conjugation. We only consider here a reciprocal transmission medium (S_{HV}=S_{VH}). Using (1), polarimetric data is represented by a set of polarimetric covariance matrices that depend on the spatial coordinates. For easing notations the spatial dependency has been dropped in (1).

Our PDE is derived to act on the elements ($\boldsymbol{C}_{ij}$) of the covariance matrix following the principles for PolSAR data filtering introduced by Lee in [3]: independent filtering of each element of the covariance matrix (co-polar S_{HH}, S_{VV}, cross-polar S_{HV}) for avoiding crosstalk between channels, use of adaptive operators for feature preservation on each channel.

We set our method to use a superposition of one-dimensional (1D) orthogonal diffusion processes acting on directions defined by a common geometry imposed through a multi-polarimetric structure tensor:

$$\boldsymbol{J}_{\rho} = G_{\rho} \sum_{i=1}^{3} \nabla \boldsymbol{C}_{\mathrm{ii}} (\nabla \boldsymbol{C}_{\mathrm{ii}})^{\mathrm{T}} \tag{2}$$

that captures and integrates in a 2 × 2 symmetric matrix the variations occurring in all the polarimetric channels. A component-wise convolution with a Gaussian function of standard deviation ρ is used to increase the robustness of this Di Zenzo driven approach [15] with respect to noise. The matrix in (2) is semi-positive definite, having eigenvectors pointing in the mean direction of the gradient vectors (**v**) and in the orthogonal, maximum homogeneity direction (**u**).

For a more efficient restoration of non-oriented regions, we further model in each pixel the orientation of the (**u**) vector as a stochastic process having as mean the associated orientation (θ_m) issued by the eigen-analysis:

$$f(\theta|\theta_m, \sigma_\theta) = \frac{1}{\sqrt{2\pi}\sigma_\theta} \exp[-\frac{\Delta(\theta, \theta_m)^2}{2\sigma_\theta^2}], \theta \in (-\frac{\pi}{2}, \frac{\pi}{2}], \tag{3}$$

with $\Delta(\theta, \theta_m)$ denoting the angular difference between the angles θ and θ_m, computed using the classic angle doubling procedure [16]. σ_θ is a parameter of the method and we choose to related it to the normalized value of the difference between the eigenvalues of (2) through a multiplicative parameter α:

$$\sigma_\theta = \alpha \cdot (1 - \frac{\mu_1 - \mu_2}{\mu_1 + \mu_2}) . \tag{4}$$

The discussion derived in [13] for the scalar image case holds also for the amplitudes of the PolSAR data. On oriented regions the orientation (θ) of the eigenvector **u** is the one issued by the multi-polarimetric tensor whereas on non-oriented regions θ takes random values drawn from a circular distribution.

Non-linear diffusion processes are usually designed to favor intra-region smoothing and to penalize inter-region smoothing. This effect is accomplished by using diffusivity functions taking as arguments the outputs of an edge detection operation. The choice of the edge detector itself for the multiplicative noise case proves to be problematic since the noise value depends on the signal amplitude. Based on recent work in edge detection [17], we use the multiplicative gradient operator to modulate the diffusion intensity along the two axes defining the diffusion geometry computed as described above. The operator is shown in [17] to provide better results than the instantaneous coefficient of variation, especially for high noise conditions and real images having a complex content. For a given 2D gray scale image (U) the multiplicative gradient $\nabla_\eta U = [\eta_x(U), \eta_y(U)]^{\mathrm{T}}$ is computed using the following formulas [13]:

$$\begin{cases} \eta_x(U) = \lim\limits_{h \to 1} (\dfrac{U(x \cdot h, y)}{U(x, y)})^{1/\ln(h)} \\ \eta_y(U) = \lim\limits_{h \to 1} (\dfrac{U(x, y \cdot h)}{U(x, y)})^{1/\ln(h)} \end{cases} . \tag{5}$$

We show in Fig. 1 the result of an edge detection operation performed on the intensity of the $\boldsymbol{S_{HH}}$ complex scattering element. All the images in Fig. 1 have been scaled in the 0–255 gray level range for a better visualization. As it can be easily noticed, in Fig. 1c the multiplicative gradient magnitude is significantly lower in homogeneous areas than in Fig. 1b (instantaneous coefficient of variation) and still high along the edges.

For capturing the features of a PolSAR image contained in all the polarimetric channels, we design our method to employ the previously described multiplicative gradient-based edge detection on the span image, which represents a weighted average of the intensities of the scattering coefficients [3, 12]:

$$\boldsymbol{S} = \text{span} = \text{trace}(C) = \left|\boldsymbol{S_{HH}}\right|^2 + 2\left|\boldsymbol{S_{HV}}\right|^2 + \left|\boldsymbol{S_{VV}}\right|^2 . \quad (6)$$

The continuous form of the PDE filter that accounts for all the above imposed properties is:

$$\frac{\partial C_{ij}}{\partial t} = \frac{\partial}{\partial \boldsymbol{v}}[g^v(\|\nabla_\eta(\boldsymbol{S})\|)\boldsymbol{C_{ij}}_v] + \frac{\partial}{\partial \boldsymbol{u}}[g^u(\|\nabla_\eta(\boldsymbol{S})\|)\boldsymbol{C_{ij}}_u] \quad (7)$$

with different diffusion functions along the axes describing the geometry of the diffusion process acting on the elements of the polarimetric scattering matrix. These functions are:

$$g^v(s) = \exp[-(s/K_v)^2] \quad (8.a)$$

and

$$g^u(s) = \frac{1}{1+s^2/K_u^2} , \quad (8.b)$$

with the K_u and K_v diffusion thresholds as parameters for our method. The choice is based on the experimental evaluation of the parameters choice for anisotropic diffusion filtering carried out in [18]. Diffusion processes driven by such functions favor high contrast edges with respect to low contrast ones, allowing on the same time adaptive smoothing along the maximum homogeneity axis (**u**). The filter corresponds to the non-regularized form of the PDE we proposed in [12]. The choice is motivated by the fact that we derive our filter to act for high resolution PolSAR images (1 meter) and we design it for avoiding pre-smoothing effects that could filter out details.

2.2. NUMERICAL APPROXIMATION SCHEME

To solve numerically equation (7) we assume a classic discretization of the time (observation scale) and the spatial coordinates: $t = ndt$, $x = ih$, $y = jh$, as in [12] and [19]. Evaluation of the right hand side of (7) is done on a moving orthonormal basis, defined in each pixel by the two axes **v** and **u**, computed as defined in equations (2) to (4). Assuming a similar spatial discretization along these axes, the numerical approximation scheme needs subpixel resolution as shown in Fig. 2 for a generic 2D function $U(x,y,t) = U(ih, jh, ndt) = U_{i,j}^n$. For easing up the notations we ignore in Fig.2 the time dependence of this function. We employ two biquadratic interpolations for computing these values on each axis by considering, respectively, $U(x,y,t)=\boldsymbol{C}_{ij}(x,y,t)$ for the system of PDEs governing the time evolution of each scattering coefficient (7).

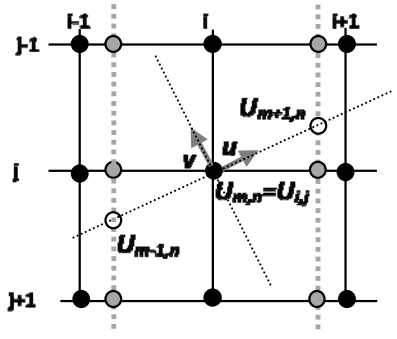

Fig. 2 – Quantities involved in the numerical approximation scheme along the **u** axis for a generic 2D function $U(x,y,t)$.

Based on these quantities we then compute the directional derivatives by using forward and backward difference operators along the **u** and **v** axes. For the generic 2D function these are:

$$\begin{aligned} D_u^{\pm}(U) &= \pm(U_{m\pm1,n} - U_{m,.n}) \\ D_v^{\pm}(U) &= \pm(U_{m,n\pm1} - U_{m,.n}) \end{aligned} \quad (9)$$

and, with these notations, the right hand side of (7) can be discretized as follows:

$$\begin{aligned} \frac{\partial C_{ij}}{\partial t} = {} & g^u[\|\nabla_\eta \boldsymbol{S}\|]\big|_{m+1/2,n} D_u^+(\boldsymbol{C_{ij}}) - g^u[\|\nabla_\eta \boldsymbol{S}\|]\big|_{m-1/2,n} D_u^-(\boldsymbol{C_{ij}}) \\ & + g^u[\|\nabla_\eta \boldsymbol{S}\|]\big|_{m,n+1/2} D_v^+(\boldsymbol{C_{ij}}) - g^u[\|\nabla_\eta \boldsymbol{S}\|]\big|_{m,n-1/2} D_v^-(\boldsymbol{C_{ij}}) \end{aligned} . \quad (10)$$

Evaluation of (10) involves evaluation of the diffusion functions at the middle of the discrete intervals $[m,m+1]$, $[m-1, m]$, $[n, n+1]$ and $[n, n+1]$. We compute these values by using simple arithmetic means between the already computed values of the span's multiplicative gradient at integer discrete coordinates m and n. These approximations lead to:

$$\begin{aligned} \|\nabla_\eta^E(\boldsymbol{S})\| &= \frac{\|\nabla_\eta(\boldsymbol{S})\|_{m,n} + \|\nabla_\eta(\boldsymbol{S})\|_{m+1,n}}{2} \\ \|\nabla_\eta^W(\boldsymbol{S})\| &= \frac{\|\nabla_\eta(\boldsymbol{S})\|_{m,n} + \|\nabla_\eta(\boldsymbol{S})\|_{m-1,n}}{2} \\ \|\nabla_\eta^N(\boldsymbol{S})\| &= \frac{\|\nabla_\eta(\boldsymbol{S})\|_{m,n} + \|\nabla_\eta(\boldsymbol{S})\|_{m,n-1}}{2} \\ \|\nabla_\eta^S(\boldsymbol{S})\| &= \frac{\|\nabla_\eta(\boldsymbol{S})\|_{m,n} + \|\nabla_\eta(\boldsymbol{S})\|_{m,n+1}}{2} \end{aligned} . \quad (11)$$

The final approximation of the right hand side term in equation (6) is:

$$\begin{aligned} \frac{\partial C_{ij}}{\partial t} = {} & g^u(\|\nabla_\eta^E(\boldsymbol{S})\|)D_u^+(\boldsymbol{C}_{ij}) - g^u(\|\nabla_\eta^W(\boldsymbol{S})\|)D_u^-(\boldsymbol{C_{ij}}) \\ & + g^v(\|\nabla_\eta^S(\boldsymbol{S})\|)D_v^+(\boldsymbol{C_{ij}}) - g^v(\|\nabla_\eta^N(\boldsymbol{S})\|)D_v^-(\boldsymbol{C_{ij}}) \end{aligned} . \quad (12)$$

The left hand side of (6) is approximated using classic forward time difference using a time step dt. The final approximation scheme that takes into account also the time discretization and the time dependence is:

$$\begin{aligned} \boldsymbol{C}_{ij}^{n+1} = {} & \boldsymbol{C}_{ij}^n + dt\cdot[g^u(\|\nabla_\eta^E(\boldsymbol{S}^n)\|)D_u^+(\boldsymbol{C}_{ij}^n) - g^u(\|\nabla_\eta^W(\boldsymbol{S})\|)D_u^-(\boldsymbol{C}_{ij}^n) + \\ & + g^v(\|\nabla_\eta^S(\mathrm{S}^n)\|)D_v^+(\mathrm{C}_{ij}^n) - g^v(\|\nabla_\eta^N(\mathrm{S})\|)D_v^-(\mathrm{C}_{ij}^n)]. \end{aligned} \quad (13)$$

2.3. PARAMETERS

The method has the following parameters: the observation scale t, the standard deviation of the Gaussian kernel used for orientation estimation (2) (ρ), the two diffusion thresholds (K_u,K_v) and the standard deviation for the stochastic process that models the orientation estimation process (σ_θ).

The parameter ρ gives the size of the orientation estimation window. For the PolSAR image classification chain we used values between 2 and 3, leading to orientation window estimation sizes from 13 × 13 to 19 × 19 pixels.

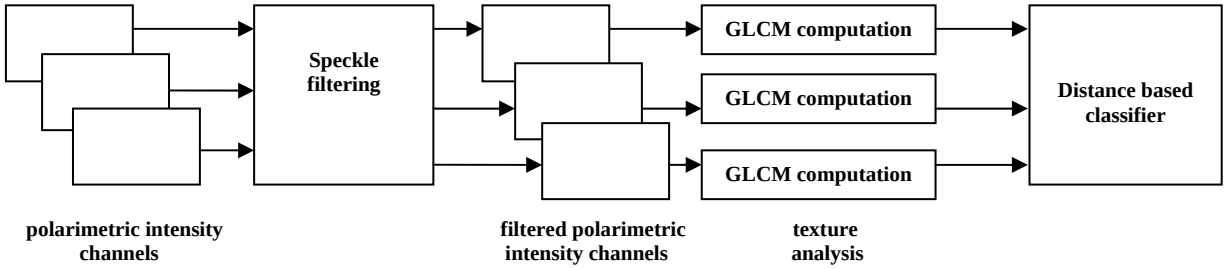

Fig.3 – PolSAR image classification chain using texture features extracted from the gray-level co-occurrence matrix of the filtered data.

The threshold parameter K_v is set to be time dependent and equal to a given percentage β of the integral value of the histogram [19] associated to the multiplicative gradient norm computed at that scale. As in [12], we set, through a multiplicative constant (α), the threshold K_u to depend linearly on K_v. The best classification results were obtained for values of β between 0.2 and 0.75, allowing for efficient edge and texture preservation. As far as α is concerned, values between 1.5 and 2 proved to be the most suitable for eliminating noise and preserving junctions. The standard deviation for the stochastic process associated with the orientation estimation process has been set as indicated in [13]. Low values (0–10) lead to less efficient restoration of regions not having a dominant orientation.

3. POLSAR IMAGE CLASSIFICATION USING TEXTURE FEATURES

The preliminary results in [12] showed that the regularized form of our method achieves very good results on denoising real and simulated PolSAR images degraded by speckle noise, comparing favorably with classic and recent despeckling approaches. Based on these results, we propose the integration of the method in a PolSAR image classification chain that employs the filtered PolSAR data for the derivation of texture features based on the gray level co-occurrence matrix and for classification using a distance based classifier. The image classification chain is the one shown in Fig. 3 and it is an extension of the solution proposed in [20] for the classification of maritime pine trees using panchromatic images, allowing for integration of a denoising step and for global validation of our novel filtering approach.

For the speckle filtering step we consider the method proposed in Section 2, with parameters tuned to keep a balance between noise elimination and texture preservation. The classification workflow filters the intensities of the scattering coefficients (i.e. the diagonal terms of the polarimetric covariance matrix (1)), extracts texture features from the filtered intensity values and classifies the underlying images based on a distance computation using a k nearest neighbor (kNN) approach.

In the texture analysis step we employ the classic gray-level co-occurrence matrix (GLCM) [21] that allows for extraction of second-order texture features:

$$\mathrm{GLCM}_d(a,b)=\sum_x\sum_y\begin{cases}1 \text{ if } I(x,y)=a \text{ and } I(x+dx,y+dy)=b\\ 0 \text{ otherwise}\end{cases}. \quad (14)$$

In (14), $I(x,y)$ is the gray level of the current pixel and $I(x+dx,y+dy)$ is the gray level of a neighboring pixel placed at a distance (dx,dy). The GLCM matrix is normalized by the number of pixels of the patches. In order to reduce the dimensionality of the classification process, to eliminate redundant information provided by the various GLCM measures, a reduced set of textural features is usually extracted from the matrix. Based on the work carried out in [20] for photometric images and in [22] for radar images, we employ for the PolSAR image case a concatenation of four texture features, namely the homogeneity, entropy, correlation and the mean gray level, averaged in four directions in the 2D image plane and normalized.

The last step uses for kNN classification the texture descriptors vectors and the Mahalanobis distance, the later allowing to account for the possible correlation among the texture feature components of these vectors.

The proposed workflow is a general one, allowing for integration of different speckle denoising methods. We evaluate the efficiency of different filters in the next section.

4. RESULTS AND DISCUSSION

The image classification workflow in Fig.3 has been tested in a real scenario that aims to automatically classify fully polarimetric SAR images representing pine tree forest stands of different ages, captured during ONERA RAMSES campaign in 2004. The image has been previously annotated and contains 62 forest stands between 5 and 48 years old pine trees that are grouped into 4 classes: less than 10 years,

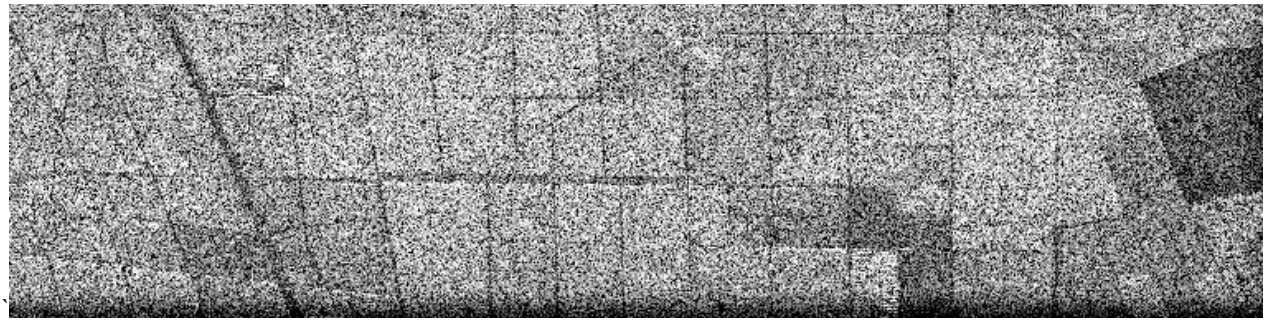

Fig. 4 – Intensity of the S_{HH} scattering coefficient for the Nezer region France (data acquired in 2004, scaled down to 8 % of the initial size).

between 11 and 20 years, between 21 and 30 years, more than 30 years. Figure 4 shows the intensity of the noisy S_{HH} scattering coefficient of the considered region, scaled on 256 gray levels.

We tested the proposed classification workflow by considering baseline filters such as box car, Gaussian convolution and special filters derived to handle the multiplicative nature of the speckle noise: the polarimetric Lee filter, the speckle reducing anisotropic diffusion method (SRAD) and our proposed method.

The different classes have been randomly partitioned into training and test classes (ratio 0.5) and 100 runs for different partitions have been tested in order to assess the accuracy of the classification process.

The best results among the three polarization channels for each filtering method are reported in Table 1.

Table 1

Classification accuracy for different filtering methods

Method	Polarimetric channel	Classification accuracy rate [%]
Unfiltered image	$\lvert S_{HH}\rvert^2$	88.03 ± 4.25
Gaussian filter	$\lvert S_{HH}\rvert^2$ ($\sigma = 0.5$)	87.00 ± 4.06
	$\lvert S_{HH}\rvert^2$ ($\sigma = 0.75$)	84.75 ± 4.00
Box car filter	$\lvert S_{HH}\rvert^2$ (3×3 pixels)	85.59 ± 4.14
	$\lvert S_{HH}\rvert^2$ (5×5 pixels)	84.22 ± 3.98
Polarimetric Lee filter[3]	$\lvert S_{HV}\rvert^2$	87.34 ±3.88
Speckle reducing anisotropic diffusion [9]	$\lvert S_{HH}\rvert^2$ ($t = 0.25$)	86.41 ±6.19
	$\lvert S_{HH}\rvert^2$ ($t = 1.0$)	80.69 ± 5.01
SAR-BM3D (SAR block-matching 3D algorithm) [8]	$\lvert S_{HH}\rvert^2$	87.50 ± 4.00
Proposed approach	$\lvert S_{HH}\rvert^2$ ($t = 1.0$)	**89.75 ± 4.00**
	$\lvert S_{HH}\rvert^2$ ($t = 1.5$)	86.71 ± 5.24

We used a cumulative distribution function-based quantization of the GLCM matrix on 256 gray levels and variable distance (1÷4).

The reported values are averages taken on the 4 directions of the numerical grid for insuring invariance with respect to orientation of the forest stands. For all the filters allowing a modulation of the smoothing intensity process two values are indicated. In the case of the Gaussian filter and the Box car filter these values correspond to the smoothing window size; for the SRAD and our method we report values at 2 observation scales (t). We also studied the influence of different k values for the kNN classifier, allowing it to vary. No significant differences were found for values between 3 and 5. For higher values the accuracy rate decreases significantly.

The GLCM classification framework shown in Fig. 3 proves to be robust even if the PolSAR data is not filtered. This is mainly due to the quantization operation that lowers the influence of the noise.

The Gaussian and the box car filters induce smoothing operations that are attenuating the influence of the noise but, on the same time, they are destroying the high frequency content associated to high resolution PolSAR images and depicting important textural forest properties, therefore, lowering the classification accuracy.

Both the polarimetric Lee filter and the speckle reducing anisotropic filter are modulating the intensity of the underlying smoothing processes by using measures (i.e. the instantaneous coefficient of variation) adapted to characterize and quantify the influence of the speckle. However, neither of these filters is capable of preserving fine texture information, leading to a slight decrease of the accuracy rate with respect to the unfiltered case.

Filtering the noisy data with the SAR-BM3D method lowers also the accuracy rate of the classification system. This is due to the method's inability to preserve texture information, as it can be seen in Fig. 5b. The result was produced with the authors own Matlab implementation [23], using the default values for all the parameters.

The filtering method proposed in Section 2 preprocesses the data by keeping a balance between noise elimination and texture preservation. The parameters were tuned for such an effect ($\alpha = 1.5$, $\beta = 0.2$), leading to the best accuracy rate in Table 1. We show in Fig. 5 details for the filtered intensity of the S_{HH} polarimetric channel using the SAR-BM3D approach and our method.

a) b) c)

Fig. 5 – Zoomed details for filtered S_{HH} channel intensity); a) original image; b) SAR BM3D result; c) result using our approach.

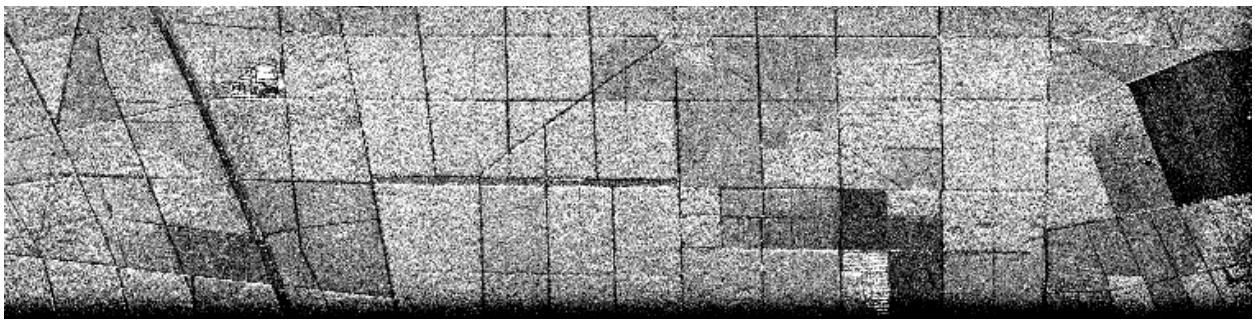

Fig. 6 – Intensity of the S_{HH} scattering coefficient filtered for better visualization with our method (scaled down to 8 % of the initial size).

As it can be seen, our approach produces results in which texture information is preserved through anisotropic, directional adaptive smoothing. Nevertheless, parameters can be tuned in order to induce a higher intensity for the smoothing process. This corresponds to higher values for the parameters α and β and to coarser observation scales (t). We show in Fig. 6 such a result. With respect to the unfiltered image (Fig. 4), contrast is enhanced, the price being paid is more loss of texture information and classification accuracy.

5. CONCLUSIONS

The paper proposes a novel directional diffusion filter for speckle noise removal that degrades the quality of polarimetric SAR images. The method is developed to integrate polarimetric information in the definition of a common diffusion geometry. The smoothing intensity on each channel is modulated by the multiplicative gradient norm, computed based on the total power of the scattered electromagnetic radiation. The method is integrated in a PolSAR image classification chain and has good results in terms of the classification accuracy. Its parameters can be also tuned for PolSAR image enhancement or restoration tasks.

Future work will be devoted for the integration of the filtered polarimetric data in a classification system that will exploit also information of the cross-polarized, non-diagonal terms of the polarimetric covariance matrix.

ACKNOWLEDEGEMENTS

This work was supported by the Executive Agency for Higher Education, Research, Development and Innovation Funding (UEFISCDI), Romania, PN II Capacitati/Module III, grant number 779/2014, and by the French Foreign Affairs and International Development Ministry through the Campus France Agency, PHC Brancusi grant number 32619VL/2015 and a SSHN (Séjours Scientifiques de Haut Niveau) program.

Received on December 17, 2016

REFERENCES

1. A. Moreira, P. Prats-Iraola, M. Younis, G. Krieger, I. Hajnsek, K.P. Papathanassiou, *A tutorial on Synthetic Aperture Radar*, IEEE Geoscience and Remote Sensing Magazine., **1**, *3*, pp. 6–43 (2013).
2. J-S. Lee, E. Pottier, *Polarimetric radar imaging: from basics to applications*, CRC Press, Taylor and Francis, 2009.
3. J-S. Lee, M.R. Grunes, G. De Grandi, *Polarimetric SAR speckle filtering and its implication for classification*, IEEE Transactions on Geoscience and Remote Sensing, **37**, *5*, pp. 2363–2373 (1999).
4. J.-S. Lee, *Refined filtering of image noise using local statistics*, Computer Vision, Graphics and Image Processing, **15**, pp. 380–389 (1981).
5. G. Vasile, E. Trouve, J-S. Lee, V. Buzuloiu, *Intensity-driven adaptive-neighborhood technique for polarimetric and interferometric SAR parameters estimation*, IEEE Transactions on Geoscience and Remote Sensing, **44**, *6*, pp. 1609–1621 (2006).
6. C.A. Deledalle, L. Denis, F. Tupin, A. Reigber, M. Jäger, *NL-SAR: A unified nonlocal framework for resolution-preserving (Pol) (In) SAR denoising*, IEEE Transactions on Geoscience and Remote Sensing, **53**, *4*, pp. 2021–2038 (2015).
7. H. Zhong, Z. Jingjing, L. Ganchao, *Robust polarimetric SAR despeckling based on nonlocal means and distributed Lee filter*, IEEE Transactions on Geoscience and Remote Sensing, **52**, *7*, pp. 4198–4210 (2014).
8. S. Parrilli, M. Poderico, C.V. Angelino, L. Verdoliva, *A nonlocal SAR image denoising algorithm based on LLMSE wavelet shrinkage*, IEEE Trans. on Geoscience and Remote Sensing, **50**, *2*, pp. 606–616 (2012)
9. A. Isar, S. Moga, D. Isar, *Denoising SONAR Images using a bishrink filter with reduced sensitivity*, Rev. Roum. Sci. Techn. – Électrotechn. et Énerg., **55**, *2*, pp.60–68 (2010).
10. Y. Yu, S. Acton, *Speckle Reducing Anisotropic Diffusion*, IEEE Transactions on Image Processing, **11**, *11*, pp. 1260–1270 (2002).
11. K. Krissian, C-F.Westin, R. Kikinis, K. Vosburgh, *Oriented speckle reducing anisotropic diffusion*, IEEE Transactions on Image Processing, **16**, *5*, pp. 1412–1424 (2007).
12. R. Terebes, M. Borda, R. Malutan, C.Germain, L. Bombrun, I. Ilea, *PolSAR image denoising using directional diffusion*, 12th International Symposium on Electronics and Telecommunications, Timisoara, Romania, 27–28 October, 2016.
13. R. Terebes, M. Borda, C. Germain, R. Malutan, I. Ilea, *A multiplicative gradient-based anisotropic diffusion approach for speckle noise removal*, E-Health and Bioengineering Conference (EHB), Iasi, Romania, 19–21 November, 2015.
14. I. Ilea, L. Bombrun, C. Germain, I. Champion , R. Terebes , M. Borda, *Statistical hypothesis test for maritime pine forest SAR images classification based on the geodesic distance*, IEEE International Geoscience and Remote Sensing Symposium (IGARSS), Milan, Italy, 26–31 July, 2015.
15. S. Di Zenzo, *A note on the gradient of a multi-image*, Computer Vision, Graphics and Image Processing, **33**, pp. 116–125 (1986).
16. K.V. Mardia, P.E. Jupp, *Directional Statistics*, John Wiley & Sons, Inc., 2000, pp. 1–7.
17. M. Mora, F. Córdova-Lepe, R. Del-Valle, *A non-Newtonian gradient for contour detection in images with multiplicative noise*, Pattern Recognition Letters, **33**, *10*, pp. 1245–1256 (2012).
18 C. Tsiotsios, M. Petroub, *On the choice of the parameters for anisotropic diffusion in image processing*, Pattern Recognition, **46** , *5*, pp. 1369–1381, (2013)
19. R. Terebes, M. Borda, S. Pop, O. Lavialle, C. Germain, C.Luduşan, *A novel diffusion filter for image restoration and enhancement*, Rev. Roum. Sci. Techn. – Électrotechn. Et Énerg., **55,** *3*, pp. 310-319, (2010).
20. O. Regniers, J-P. Da Costa, G. Grenier, C. Germain, L.Bombrun, *Texture based image retrieval and classification of very high resolution maritime pine forest images*, IEEE International Geoscience and Remote Sensing Symposium, Melbourne, Australia, July, 2013.
21. R.M Haralick, K. Shanmugam, I. Dinstein, *Textural features for image classification*, IEEE Trans. Syst., Man, Cybern., Syst., **6**, pp. 610–621 (1973).
22. I. Champion., Ch. Germain, JP. Da Costa, A. Alborini, P. Dubois-Fernandez, *Retrieval of forest stand age from SAR image texture for varying distance and orientation values of the Grey Level Co-occurrence Matrix*, IEEE Geosciences and Remote Sensing Letters, **11**, *1*, pp. 5–9 (2014) .
23. GRIP Image processing research group, SAR BM3D reference implementation http://www.grip.unina.it/web-download.htlm?dir=JSROOT/SAR-BM3D [accessed 1.09.2016]